Physics of Thin Film Formation in Microchannels: New Physical Insights and Governing Correlations

Abdolreza Fazeli, Meisam Habibi Matin, and Saeed Moghaddam*
Department of Mechanical and Aerospace Engineering
University of Florida
Gainesville, FL, USA, 32611
E-mail: saeedmog@ufl.edu

ABSTRACT

Thin film evaporation is a prominent mechanism of heat transfer in the microchannel flow boiling process, and numerous studies have attempted to predict its contribution to the overall surface heat transfer. In this study, a novel experimental platform capable of producing microscale data with unprecedented spatial and temporal resolutions is utilized to determine the liquid film thickness formed around an elongated bubble. A model is developed to accurately predict surface heat transfer during the thin film evaporation process. First, it is shown that thin film formation and evaporation can be represented in two stages: 1) adiabatic formation of the liquid layer followed by 2) thermal development and evaporation of the liquid film. It is then explained how the liquid layer thickness is affected by the flow parameters.

KEY WORDS: Thin film formation, Two-phase flow, Microchannels, Thin film evaporation

NOMENCLATURE

P	Pressure, kPa
T	Temperature, °C
$\dot{m}$	Mass flux, kg/m^2.s
k	Thermal conductivity, W/m.K

Greek symbols

δ	Liquid thickness (μm)

Subscripts

s	Surface
evap.	Evaporation

INTRODUCTION

The ever-increasing generation of waste heat has become an impediment to advancements and efficient operation of many electronics and energy applications, such as power and RF electronics, high performance computers, and solid-state lasers. Significant research over the past couple of decades has focused on improving efficacy of two-phase cooling systems considered as a potential solution for thermal management of the mentioned applications [1]–[5].

Advancement of the two-phase cooling technology requires fundamental understanding of the two-phase flow heat transfer at microscale which includes interfacial interactions between the phases that govern the flow thermal and hydrodynamic characteristics. Historically, the flow within a microfluidic multiphase system has been considered dominated by viscous forces, while the inertial effects are considered negligible. This definition supposedly simplifies the transport phenomena and facilitates its analysis in microchannels. However, despite many years of research [6]–[9], a detailed explanation of physics of heat and mass transfer and interactions between phases in microchannels has yet to be presented. A key challenge in deciphering this process is the lack of understanding of formation and evaporation mechanism of thin liquid layers on the channel walls.

The common approach in studying the liquid layer thickness (and profile) and evaluating its associated hydrodynamic and thermal behavior is analytical and numerical. Following the pioneering work by Bretherton [10], researchers attempted to characterize the liquid layer formed around a moving bubble in microchannels by solving a simplified form of Navier-Stokes equations for multiphase flow in microchannels [11]–[13]. The results of these comprehensive studies shed light on effects of various parameters such as vapor/gas velocity, surface tension and viscosity on the liquid film thickness. A major drawback associated with these studies is assuming a simplified case of fully developed, one dimensional liquid-vapor interface within the channel. This model disregards effects of lateral and longitudinal mass transfer within the liquid layer and does not capture transient characteristics of the process.

In this work, we utilize a thermal-based measurement technique to characterize liquid films formed around elongated bubbles in microchannels. The new approach allows resolving surface thermal events with unparalleled spatial and temporal resolutions. The experimental data coupled with numerical and analytical studies have enabled deciphering the physics of liquid films formation and evaporation.

EXPERIMENTAL SETUP

A detailed view of an experimental setup and a microfluidic chip used in this study are presented in Figure 1. The device consists of a single rectangular microchannel with inlet and outlet ports for fluid entry and exit. The microchannel wall is made of a 75 μm-thick SU8 film and is sealed by a Polydimethylsiloxane (PDMS) transparent cap. The microchannel width is 300 μm. After the inlet port, there is a pre-heater section in which the working fluid is heated up to the desired temperature before entering the test section.

The bottom surface of the channel is made of a thick high thermal conductivity material (a 500-μm thick silicon substrate) coated with a low thermal conductivity film (a 9.8-μm thick layer of SU8). At the Su8-liquid interface, the test section is covered with 51 resistance temperature detectors (RTDs), while 3 RTDs are sputter deposited at the Si-Su8

interface to measure the temperature distribution during the boiling process. Several thin film heaters are also embedded at the SU8-silicon interface that provide heat to the flow.

The microfluidic chip is wire-bonded to a custom made printed circuit board (PCB) to transfer the temperature data to the data acquisition (DAQ) system. The DAQ system consists of a current excitation, a channel amplifier module and a high speed DAQ module and can record temperature data at a frequency of 20 kHz. A high-speed camera (FASTCAM SA4-Photron) is synchronized with the DAQ to visualize the boiling process at a frequency of 20k frames per second.

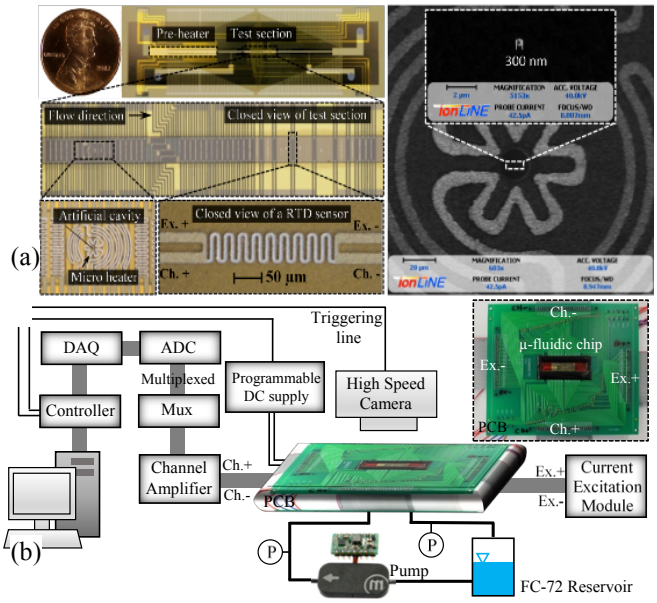

Fig. 1 (a) detailed view of the microfluidic chip (test section, pre-heater, artificial cavity and pulsed function microheater), (b) schematic of experimental loop (inset figure shows the wire bonded device to PCB)

The working fluid is delivered to the microfluidic chip by a piezoelectric micropump (Model MP6, manufactured by Bartels Mikrotechnik GmbH). Two PX-26 pressure transducers with ±1% reading error are used to measure the pressure drop along the microchannel. The working fluid is degassed by vigorous boiling for several hours before each experiment. Then, the desired surface temperature is adjusted and allowed about 15 minutes to reach a steady state before recording the data.

EXPERIMENTAL RESULTS

Using the experimental setup discussed in the previous section, single bubbles are generated at a desired frequency at an artificial nucleation site. Bubbles grow and pass over the sensor array (cf. Fig. 2).

The sensor array captures thermal events with sub-millisecond timescale, a task that has been impossible to accomplish using experimental techniques utilized in prior multiphase studies [14]–[17]. A typical set of experimental data recorded as an elongated bubble passes over the sensor array in presented in Fig. 3.

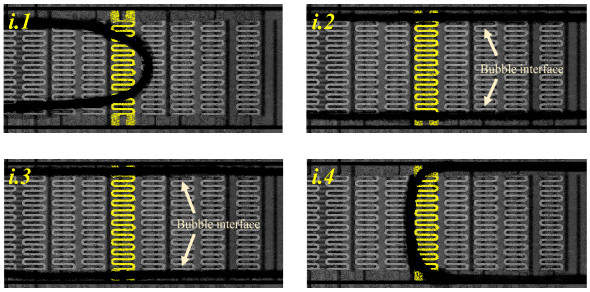

Fig. 2 High speed imaging of a moving bubble as it passes over the surface (Sensor 35 is highlighted on the surface). i.1) bubble tip reaches the sensor (point A in Fig. 3), i.2-3) bubble is covering most of channel width and liquid layer on the side is thinning, i.4) bubble end passes over the sensor (point E in Fig. 3)

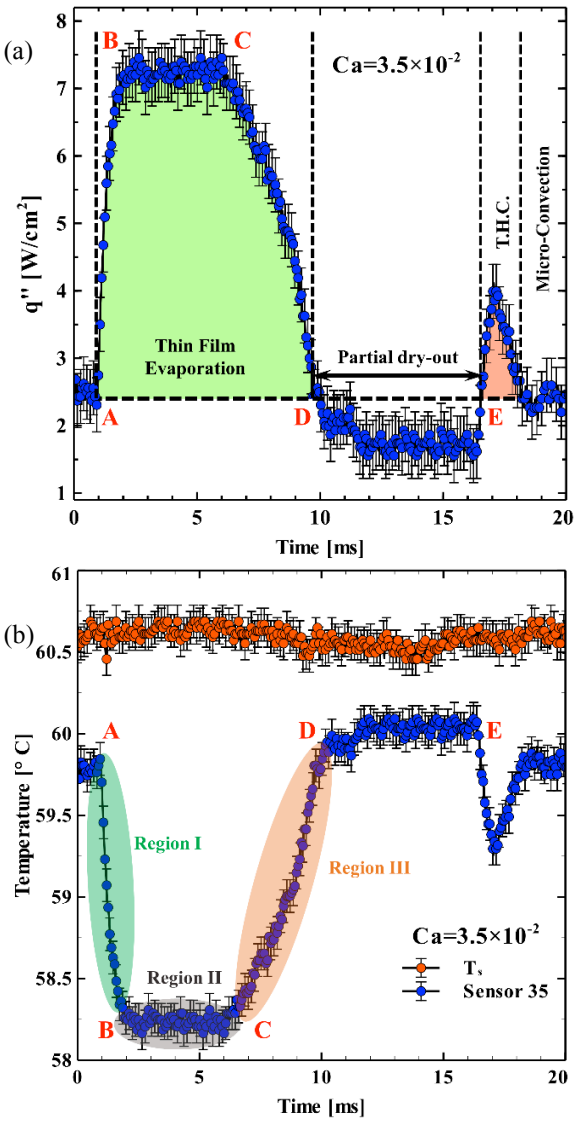

Fig. 3 Experimental results as a function of time measured at S35. (a) Local heat flux values help identify the respective heat transfer mechanisms associated with a moving bubble over a sensor, (b) Temperature values recorded as a function of time show three distinct regions during thin film evaporation mode of heat transfer

Three distinct thermal events are identified as the bubble moves over the sensor array [18], [19]: thin film evaporation, surface dry-out (partially or fully), and transient heat conduction (cf. Fig 3a). The thin film evaporation mode of heat transfer initiates as the front side of the bubble reaches the sensor. This stage is identified as point A on Fig. 3b, corresponding to a sudden increase in surface heat flux. This abrupt change in heat flux is due to evaporation of a thin liquid film formed underneath the bubble. Following the initial spike, the local heat flux remains relatively constant for 5-10 milliseconds, depending on different flow conditions. The onset of this event is marked as point B. After this period, heat flux declines and surface eventually experiences partial dry-out. The onset of partial dry-out is marked as point D. Finally, as the rear end of the bubble draws closer and the liquid slug trailing the bubble rewets the sensor, the local heat flux rapidly inclines (point E). This process known as "transient heat conduction" has been discussed in our prior publications [18], [20], [21]. The local heat flux then gradually declines and reaches a steady state condition corresponding to the single phase heat transfer regime. The single-phase heat transfer coefficient is experimentally calculated to be $h_{experimental}$ ~3900 W/m^2 K, which is less than 15% different from the analytical value of $h_{analytical}$ ~3300 W/m^2 K (corresponding to a Nusselt number of 6.2 [18]).

The focus of this work is to evaluate the thin film evaporation period (cf. Fig. 3a), that involves significant interfacial heat and mass transfer, and explain the thermal and hydrodynamic interactions between the liquid layer and the vapor core.

Analysis of thin film evaporation process

The results suggest that during the thin film evaporation process three separate regions (cf. Fig. 3) can be identified:

1. Region I: the bubble front has reached the sensor and caused a significant increase in the surface heat flux as well as a sudden drop in surface temperature.
2. Region II: the surface temperature reached its minimum value, a quasi-steady condition started during which temperature and heat flux remained constant for a short period of time.
3. Region III: as the liquid film dried out, the surface temperature gradually increased until it reached its maximum value.

In the following, we utilize the experimental data recorded in individual regions to explain different stages associated with formation, thermal development and evaporation of the liquid layer.

Region I: Formation and development of thin films

As the bubble's front reached the sensor, the surface temperature suddenly dropped and the recorded heat flux increased (within a time period of ~ 1ms as shown in Fig. 3). This trend is indicative of transition from single phase to thin film evaporation mode of heat transfer due to the formation of the liquid layer [18]. The focus of this section is to present a detailed description of the transient behavior of liquid layer forming around the bubble.

The bubble images (cf. Fig. 2) show that the front side of the bubble moves at a velocity of ~1 m/s. At this speed, it takes approximately 50 μs for it to pass over Sensor 35 and form the liquid film (with a thickness of δ_0). This time period is two orders of magnitude shorter than the evaporation time of the liquid film (~10 ms) and its associated input heat flux is calculated to be approximately 0.3% of the evaporation period. Hence, the amount of heat transferred into the liquid film and change in its thickness (due to evaporation) is considered negligible.

After the liquid film has formed on the surface, it starts to thermally develop until reaching the quasi-steady condition (i.e. point B in Fig. 3a). The initial temperature of the film can be readily determined using the surface temperature and heat flux data. The temperature profile within the film is that of a few microns thick layer of liquid carved from the liquid slug present on the surface before the film formation. This temperature profile is assumed to be linear $T(y) = T_s - q''\delta(y)/k$, as correctly done by Thome et al. [22].

The next step in analyzing the film is to determine the transient thickness of formed liquid layer (denoted by δ_{R-I}) and its associated initial temperature profile. Using this description, $\delta_{R-I}(t)$ was back-calculated from δ_{R-II} (i.e. the thickness of liquid layer of region II, which reached a quasi-steady temperature profile, and is equal to $\delta_{R-II} = k\Delta T / q''$), such that:

$$\delta_{R\text{-}I}(t) = \delta_{R\text{-}II} + \int_t^{t_B} \left(-\partial\delta/\partial t\right) dt \quad (1)$$

Where $\partial\delta/\partial t = -q''/\rho h_{fg}$ is calculated numerically by using the experimental heat flux data presented in Fig. 3a. The difference between $\delta_{R\text{-}I}$ and $\delta_{R\text{-}II}$ was then measured as a function of time and is shown in Fig. 4.

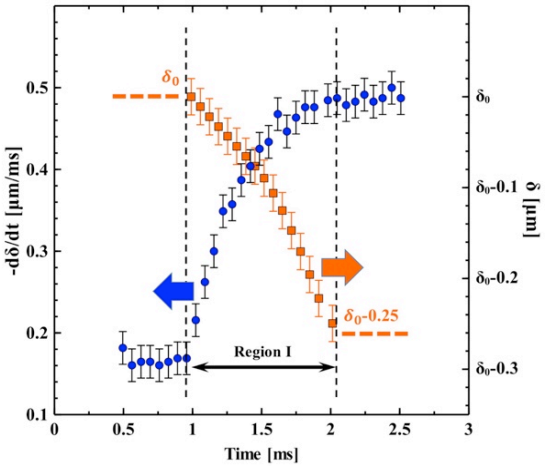

Fig. 4 The change in liquid layer thickness and its slope as a function of time

To validate the procedure discussed above, a set of numerical simulations was conducted and the resulted were compared with the experimental data in Fig. 5. The comparison shows a reasonable match between the experimental and numerical data.

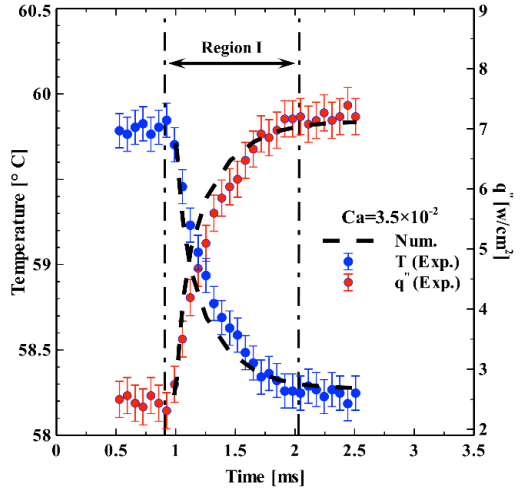

Fig. 5 Comparison between simulation results & experimental values for surface temperature and heat flux as a function of time

Region II: Quasi-steady thin films

The Region II process initiated as the temperature profile in the liquid layer reached its quasi-steady state (cf. Fig. 3b). The surface temperature and heat flux leveled out for several milliseconds. The relatively constant heat flux and surface temperature observed in this region implies that the liquid film thickness should also remain constant (cf. $\delta_{R\text{-}II} = k(T_s\text{-}T_{sat})/q"$). Therefore, liquid must have been continuously delivered to the heated area to compensate for the evaporation caused by the applied heat flux ($\dot{m}_{delivered} = \dot{m}_{evaporated} = q"/h_{fg}$). To determine the liquid source, it was hypothesized that there could be only three paths for the liquid around the bubble to feed the evaporating liquid film. Fig. 6 depicts these paths:

$$\dot{m}_{delivered} = \dot{m}_f + \dot{m}_{w,f} + \dot{m}_{w,s} \quad (2)$$

$\dot{m}_f$ represents the liquid film flowing along with the bubble due to pressure gradient along the channel and shear forces applied by vapor phase. $\dot{m}_{w,f}$ and $\dot{m}_{w,s}$ represent liquid wicking due to the capillary pressure generated on front and sides of the bubble, respectively.

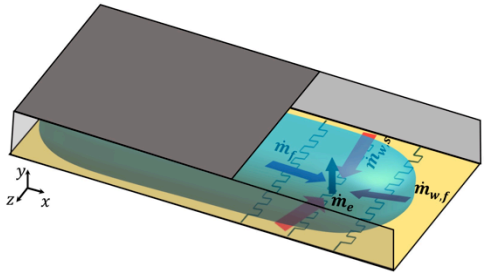

Fig. 6 Liquid delivery mechanisms to the liquid film beneath the bubble

The analysis presented below suggests that $\dot{m}_{w,s}$ is almost entirely responsible for continuous feeding of the thin film over the sensor area. $\dot{m}_f$ was estimated by solving the Navier-Stokes equation and finding an approximate solution for the velocity profiles of liquid and vapor phases. The results suggested that for a ~2-μm-thick liquid film formed underneath the bubble, $\dot{m}_f$ is negligible.

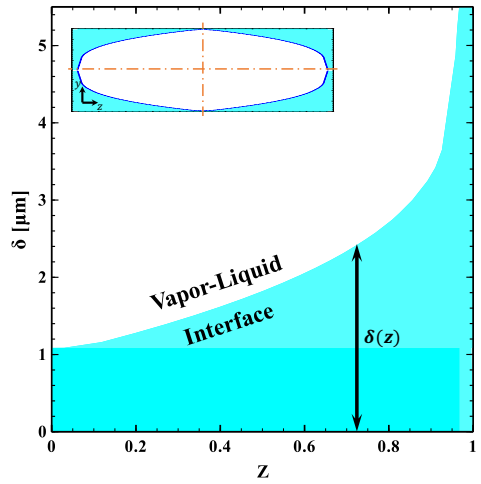

Fig. 7 bubble cross-sectional interface reconstructed using numerical simulations results (the cross-sectional view is not to scale)

It is then concluded that capillary action should be the main mechanism responsible for much of liquid delivery in Region II. In a capillary driven flow, the change in radius of curvature at liquid-vapor interface generates a capillary pressure ($P_C = \sigma \times \delta" / \left[1 + \delta'^2\right]^{3/2}$, δ denotes the liquid layer thickness), which induces the liquid flow ($\dot{m}_{wick} = {}^{\rho}/_{\mu} \times {}^{dP_c}/_{dx} \times {}^{\delta^3}/_{3}$). To estimate the wicking mass flux in the flow direction ($m_{w,f}$), the capillary pressure gradient was first experimentally calculated using the directional derivatives of thin film thickness. Evidently, there was no noticeable variation in thickness of the liquid layer in the flow direction, implying that the slope and curvature of the meniscus over the width of three sensors (~350μm) were almost zero. The capillary pressure and the liquid flow in the streamwise direction were thus insignificant (P_c & $m_{w,f}$~0).

Consequently, for the liquid film thickness to remain constant, the transversal wicking mass flux ($\dot{m}_{w,s}$) was determined to be responsible for replenishing the liquid film. A closer look at the bubble images (compare Figs. 2.2 and 2.4) clearly shows that the thickness of a body of liquid left at the sides of the bubble continuously declines indicating the flow of liquid in the z-direction. The mass balance equation for the evaporating liquid film was then reformulated as: $m_{evap.} - m_{w,s} \cong 0$. The solution to this set of equations enabled determining the shape of the liquid-vapor interface (cf. Fig. 7).

Liquid thickness measurement around the bubble.

The thickness of liquid layer underneath (δ_V) and on the sides (δ_H) of bubble is calculated using the experimental data for different flow conditions and surface temperatures (cf. Fig. 8).The results suggest that, because the channel geometry is rectangular, δ_V is different than δ_H. But, the more important result is that δ_H increased with capillary number (Ca) while δ_V remained almost independent of Ca. The Bretherton's model [10], on which Thome et al. [22] have based their model, and similar models [23]–[27] are unable to predict a film thickness

independent of Ca. Bretherton [10] developed his model based on simple fluid dynamics concepts; the lubrication theory in an axisymmetric 2D (i.e. circular) channel. The correlation he proposed relates the film thickness to the capillary number as $\delta/R = 1.34Ca^{2/3}$.

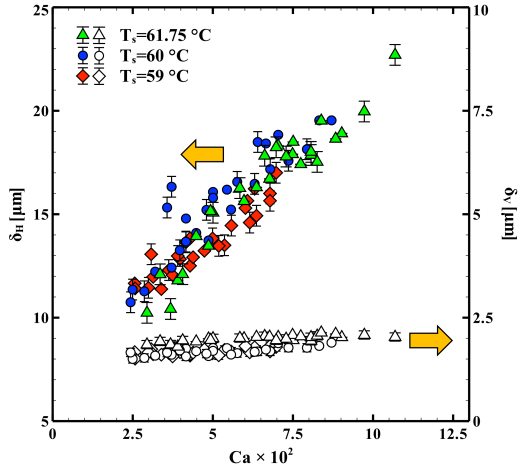

Fig. 8 Variation of liquid layer thickness underneath (δ_V) and around (δ_H) the bubble as a function of capillary number at different surface temperatures

Region III: Thin film termination

The final region in the thin film evaporation process initiates as the available liquid on the side of the bubble diminishes. At this condition, the capillary mass flux could no longer compensate for the evaporating mass flux and surface of the sensor starts to dry out. The vapor, now directly in contact the surface, acts as a thermal insulator ($k_{FC\text{-}72,vapor} << k_{FC\text{-}72,liquid}$), causing significant increase in surface temperature.

CONCLUSIONS

In this study, a unique thermographic technique was utilized to study the formation and evaporation mechanisms of thin liquid films beneath a moving bubble in a microchannel. Details of the process were captured with unprecedented spatial and temporal resolutions. The data clearly shows that thin film formation timescale is an order of magnitude shorter than its evaporation timescale. Three individual regimes were identified and studied during the formation and evaporation process. These regimes include formation, thermal development and evaporation of the liquid film.

A fascinating outcome of the experimental measurements and analysis was to determine the role of channel geometry and capillary number on the thickness of liquid layer and thus thermal characteristics of the two-phase flow. We have shown that, contrary to common opinion [10], [23]–[27], liquid layer thickness around the bubbles can be independent of capillary number in rectangular microchannels.

ACKNOWLEDGMENTS

This study was supported by a grant from the National Science Foundation (NSF) under contract CBET-1403657. Fabrication of the devices was conducted in the Nanoscale Research Facility (NRF) at the University of Florida.

References

[1] A. Fazeli and S. Moghaddam, "A New Paradigm for Understanding and Enhancing the Critical Heat Flux (CHF) Limit," *Sci. Rep.*, vol. 7, no. 1, p. 5184, Dec. 2017.

[2] A. Fazeli, M. Mortazavi, and S. Moghaddam, "Hierarchical biphilic micro/nanostructures for a new generation phase-change heat sink," *Appl. Therm. Eng.*, vol. 78, no. 0, pp. 380–386, Mar. 2015.

[3] A. Fazeli, S. Bigham, and S. Moghaddam, "Microscale layering of liquid and vapor phases within microstructures for a new generation two-phase heat sink," *Int. J. Heat Mass Transf.*, vol. 95, pp. 368–378, Apr. 2016.

[4] D. Li, G. S. Wu, W. Wang, Y. D. Wang, D. Liu, D. C. Zhang, Y. F. Chen, G. P. Peterson, and R. Yang, "Enhancing flow boiling heat transfer in microchannels for thermal management with monolithically-integrated silicon nanowires.," *Nano Lett.*, vol. 12, no. 7, pp. 3385–90, Jul. 2012.

[5] D. Cooke and S. G. Kandlikar, "Effect of open microchannel geometry on pool boiling enhancement," *Int. J. Heat Mass Transf.*, vol. 55, no. 4, pp. 1004–1013, Jan. 2012.

[6] A. Günther, S. a Khan, M. Thalmann, F. Trachsel, and K. F. Jensen, "Transport and reaction in microscale segmented gas-liquid flow.," *Lab Chip*, vol. 4, no. 4, pp. 278–86, Aug. 2004.

[7] M. T. Kreutzer, F. Kapteijn, J. A. Moulijn, and J. J. Heiszwolf, "Multiphase monolith reactors: Chemical reaction engineering of segmented flow in microchannels," *Chem. Eng. Sci.*, vol. 60, no. 22, pp. 5895–5916, Nov. 2005.

[8] H. Song, D. L. Chen, and R. F. Ismagilov, "Reactions in Droplets in Microfluidic Channels," *Angew. Chemie Int. Ed.*, vol. 45, no. 44, pp. 7336–7356, Nov. 2006.

[9] S. Bigham and S. Moghaddam, "Physics of the Microchannel Flow Boiling Process and Comparison With the Existing Theories," *J. Heat Transfer*, vol. 139, no. 11, p. 111503, Jun. 2017.

[10] F. P. Bretherton, "The motion of long bubbles in tubes," *J. Fluid Mech.*, vol. 10, no. 2, p. 166, Mar. 1961.

[11] J. Ratulowski and H.-C. Chang, "Marangoni effects of trace impurities on the motion of long gas bubbles in capillaries," *J. Fluid Mech.*, vol. 210, no. 1, p. 303, Jan. 1990.

[12] H. Wong, C. J. Radke, and S. Morris, "The motion of long bubbles in polygonal capillaries. Part 1. Thin films," *J. Fluid Mech.*, vol. 292, no. 1, p. 71, Jun. 1995.

[13] A. Oron, S. H. Davis, and S. G. Bankoff, "Long-scale evolution of thin liquid films," *Rev. Mod. Phys.*, vol. 69, no. 3, pp. 931–980, Jul. 1997.

[14] P. Garstecki, I. Gitlin, W. DiLuzio, G. M. Whitesides, E. Kumacheva, and H. A. Stone, "Formation of monodisperse bubbles in a microfluidic flow-focusing device," *Appl. Phys. Lett.*, vol. 85, no. 13, pp. 2649–2651, Sep. 2004.

[15] J. J. Heras, A. J. Sederman, and L. F. Gladden, "Ultrafast velocity imaging of single- and two-phase

flows in a ceramic monolith," *Magn. Reson. Imaging*, vol. 23, no. 2, pp. 387–389, Feb. 2005.

[16] M. A. Le Gros, G. McDermott, and C. A. Larabell, "X-ray tomography of whole cells," *Curr. Opin. Struct. Biol.*, vol. 15, no. 5, pp. 593–600, Oct. 2005.

[17] J. H. Kinney and M. C. Nichols, "X-Ray Tomographic Microscopy (XTM) Using Synchrotron Radiation," *Annu. Rev. Mater. Sci.*, vol. 22, no. 1, pp. 121–152, Aug. 1992.

[18] S. Bigham and S. Moghaddam, "Microscale study of mechanisms of heat transfer during flow boiling in a microchannel," *Int. J. Heat Mass Transf.*, vol. 88, pp. 111–121, Sep. 2015.

[19] S. Bigham and S. Moghaddam, "Role of bubble growth dynamics on microscale heat transfer events in microchannel flow boiling process," *Appl. Phys. Lett.*, vol. 107, no. 24, p. 244103, 2015.

[20] S. Moghaddam and K. Kiger, "Physical mechanisms of heat transfer during single bubble nucleate boiling of FC-72 under saturation conditions-I. Experimental investigation," *Int. J. Heat Mass Transf.*, vol. 52, no. 5–6, pp. 1284–1294, Feb. 2009.

[21] S. Moghaddam and K. Kiger, "Physical mechanisms of heat transfer during single bubble nucleate boiling of FC-72 under saturation conditions. II: Theoretical analysis," *Int. J. Heat Mass Transf.*, vol. 52, no. 5–6, pp. 1295–1303, Feb. 2009.

[22] J. R. Thome, V. Dupont, and a.M. Jacobi, "Heat transfer model for evaporation in microchannels. Part I: presentation of the model," *Int. J. Heat Mass Transf.*, vol. 47, no. 14–16, pp. 3375–3385, Jul. 2004.

[23] F. Fairbrother and A. E. Stubbs, "119. Studies in electro-endosmosis. Part VI. The 'bubble-tube' method of measurement," *J. Chem. Soc.*, pp. 527–529, 1935.

[24] R. N. Marchessault and S. G. Mason, "Flow of Entrapped Bubbles through a Capillary," *Ind. Eng. Chem.*, vol. 52, no. 1, pp. 79–84, Jan. 1960.

[25] S. Irandoust and B. Andersson, "Liquid film in Taylor flow through a capillary," *Ind. Eng. Chem. Res.*, vol. 28, no. 11, pp. 1684–1688, Nov. 1989.

[26] J. Bico and D. Quéré, "Liquid trains in a tube," *EPL (Europhysics Lett.*, vol. 51, no. 5, p. 546, 2000.

[27] P. Aussillous and D. Quéré, "Quick deposition of a fluid on the wall of a tube," *Phys. Fluids*, vol. 12, no. 10, p. 2367, 2000.